Journal of
Materials Chemistry B

PAPER

View Article Online
View Journal

Cite this: DOI: 10.1039/d6tb00705h

Extracellular vesicle-integrated gelatin sponges enhance angiogenesis and cell migration in wound healing

Elif Conger-Onder,[ab] Sukru Ozturk,[a] Naside Mangir,[c] Alp Can[d] and Kezban Ulubayram*[ab]

Received 28th March 2026,
Accepted 25th May 2026

DOI: 10.1039/d6tb00705h

rsc.li/materials-b

Wound healing remains a major global burden on healthcare systems. Extracellular vesicle (EV)-based therapies have emerged as promising cell-free approaches due to their ability to deliver bioactive cargo. However, their clinical transition is largely limited by the lack of effective delivery systems for preserving EV stability and bioactivity at the target site following administration. Herein, we present clinically relevant, biocompatible and biodegradable gelatin sponges (GS) as a functional biomaterial platform for EVs derived from rat bone-marrow mesenchymal stromal cells (rt-BM-MSCs). The GS was fabricated *via* glutaraldehyde crosslinking, followed by lyophilization, to obtain a stable and highly porous architecture suitable for EV loading. This intrinsic porous structure enabled efficient EV loading and incorporation within the scaffold. Biological function assays demonstrated that the incorporation of EVs into the GS preserved and supported their biological activities, particularly by enhancing keratinocyte migration, a key process in re-epithelialization during wound healing. The pro-angiogenic potential of the EV-integrated GS was further evaluated using *ex vivo* aortic ring and *ex ovo* chorioallantoic membrane (CAM) assays, which mimic microvascular sprouting and functional vascular network, respectively. In both models, the EV-integrated GS significantly promoted neovascularization, providing functional validation beyond conventional *in vitro* assays. These models provided physiologically relevant evidence of vascularization, a key process underlying granulation tissue formation and wound repair. Importantly, GS integration enhanced EV efficacy, indicating that the biomaterial microenvironment actively modulates EV bioactivity and improves angiogenic outcomes.

1. Introduction

Wound healing treatments have made significant progress; however, chronic and complex wounds continue to pose a major clinical challenge, constituting a significant social and economic burden on healthcare systems. This burden is expected to escalate globally with the increasing elderly population.[1] Advanced therapeutic approaches, including cell-based therapies and tissue-engineered skin constructs, have emerged as promising strategies for the treatment of chronic and complex wounds.[2,3] Nevertheless, these interventions still face considerable limitations, such as uncontrolled stem cell differentiation, restricted donor availability, and the risk of adverse immune reactions, all of which hinder their broad clinical translation.[4]

Wound healing is a highly coordinated and dynamic biological process involving multiple cell types and molecular pathways. This process proceeds through the sequential and overlapping phases of hemostasis, inflammation, proliferation, maturation, and remodeling. Among these, angiogenesis, the formation of new blood vessels from pre-existing vasculature, plays an important role throughout all stages of tissue repair. From the proliferative phase to the remodeling phase, angiogenesis supports the formation of granulation tissues and ensures adequate oxygen and nutrient delivery to sustain cellular proliferation and migration.[5] Given this, insufficient or impaired angiogenesis is a major contributor to delayed or non-healing wounds.[6] Thus, strategies to enhance angiogenesis through exogenous stimuli have gained significant research attention. In this context, extracellular vesicles (EVs) represent a promising therapeutic candidate. EVs are heterogeneous, lipid bilayer-enclosed particles secreted by all eukaryotic

---

[a] *Department of Basic Pharmaceutical Sciences, Faculty of Pharmacy, Hacettepe University, Ankara, 06230, Turkey. E-mail: ukezban@hacettepe.edu.tr*
[b] *Bioengineering Division, Institute for Graduate Studies in Science and Engineering, Hacettepe University, Ankara, 06800, Turkey*
[c] *Department of Urology, Faculty of Medicine, Hacettepe University, Ankara, 06230, Turkey*
[d] *Department of Histology and Embryology, Faculty of Medicine, Ankara University, Ankara, 06230, Turkey*

and prokaryotic cells under physiological and pathological conditions.[7,8] Notably, EVs have been reported to exhibit therapeutic capacities comparable to those of their parent stem cells while potentially offering advantages in safety and clinical applicability.[9] EVs have functional effects across all stages of the wound healing processes,[10,11] including the establishment and maturation of a functional vascular network within the wound microenvironment.[12] This involvement is tightly regulated in coordination with other wound healing phases. Furthermore, EVs have been shown to facilitate intercellular communication between endothelial cells and various stromal cell types within the wound site, thereby amplifying angiogenic signaling and enhancing overall tissue repair.[13] Despite the abundance of EV-based wound healing studies, effective delivery strategies that stabilize EVs and enhance their angiogenic function within the wound microenvironment remain limited. Addressing this gap is essential, as angiogenesis directly influences the quality of granulation tissue and the overall healing process. Therefore, maintaining EV stability and preserving their biological cargos are essential. Incorporating EVs into carrier systems protects them from enzymatic degradation and systemic clearance mechanisms, thereby enhancing their stability and bioavailability.[14] Additionally, encapsulation enables the localized concentration of EVs at the injury site, leading to elevated levels of bioactive components and improved therapeutic outcomes.[15] In the present study, EVs are integrated into gelatin sponges (GS) to preserve their biological activity while also providing a structural scaffold for potential wound healing applications.

Gelatin, a natural polymer derived from the partial hydrolysis of collagen, exhibits inherent biocompatibility and biodegradability. Gelatin-based biomaterials have been widely used as scaffolds in tissue engineering, supporting cell adhesion, proliferation, and differentiation, thereby contributing to effective wound closure and tissue regeneration. Clinically, GS is commonly used as a hemostatic agent and can be fabricated under mild conditions with tunable physical properties. Notably, growth factor–loaded GS has been shown to provide controlled release at the wound site and enhance therapeutic outcomes while minimizing systemic side effects.[16] These characteristics collectively support the suitability of GS as an effective carrier system for EV delivery.

In this study, we investigate the functional *in vitro* and angiogenic potential of EVs isolated from rat bone-marrow mesenchymal stromal cells (rt-BM-MSCs) by incorporating them into GS for applications in angiogenesis-mediated wound healing. Following isolation and characterization, their effects on keratinocyte (HaCaT) proliferation and migration are evaluated under both free-EV and GS-integrated conditions. Furthermore, angiogenic potential is assessed *via* an *ex vivo* aortic ring for microvascular sprouting and *ex ovo* chorioallantoic membrane (CAM) assays for functional vessel density. The findings demonstrate that GS can function as a biomaterial platform that preserves and modulates EV bioactivity while enhancing its angiogenic performance. Overall, this study offers a potential translational strategy for EV-based wound healing therapies.

2. Materials and methods

2.1. Extracellular vesicle isolation and characterization

rt-BM-MSCs were isolated from 3- to 8-week-old male Wistar albino rats following a previously established protocol.[17] Prior to the procedure, the rats were euthanized by cervical dislocation. Under aseptic conditions, the femur and tibia from both hind limbs were excised and transferred to the laboratory in α-MEM (Cegrogen®, Germany) supplemented with 10% FBS (Sigma Aldrich, USA), 1% L-glutamine (Cegrogen®, Germany), and 1% penicillin–streptomycin (Cegrogen®, Germany). After washing the bones with PBS containing 1% penicillin–streptomycin and gentamicin (Cegrogen®, Germany), bone marrow aspirates were obtained by flushing the medullary cavity with a medium using a 10 mL syringe. The collected bone marrow suspension was then passed through a cell strainer and centrifuged three times at 170×*g* for 5 minutes to remove debris and obtain a purified cell pellet. After washing the cells by centrifugation, the resulting cell pellet was resuspended in α-MEM (Cegrogen®, Germany) supplemented with 10% (v/v) FBS, 1% L-glutamine, and 0.1% penicillin–streptomycin (Cegrogen®, Germany) and subsequently seeded into cell culture flasks. EVs were isolated from rt-BM-MSCs at passage 4 as described below. When the cultures reached 60–70% confluency, the medium was replaced with serum-free α-MEM, following a PBS wash, and the cells were incubated for an additional 48 hours. Conditioned media were then collected for EV isolation.

For EV purification, conditioned media were sequentially centrifuged at 300×*g* for 10 minutes to remove cell debris, 2000×*g* for 20 minutes to eliminate apoptotic bodies, and 10 000×*g* for 40 minutes to remove microvesicles (Optima XPN-100 Ultracentrifuge, Beckman Coulter, USA). The resulting supernatant, enriched in small EVs, was ultracentrifuged at 100 000×*g* for 120 minutes to pellet the vesicles. The pellet was washed once with PBS and subjected to a second ultracentrifugation at 100 000×*g* for 120 minutes. All centrifugation steps were performed at 4 °C. Both fixed-angle 45 Ti (*k*-factor: 133) and swing-out SW32 Ti (*k*-factor: 204) rotors (Beckman Coulter, USA) were used during the isolation process. The final EV pellet was resuspended in PBS, and the preparations were stored at −80 °C until further use.

Isolated EVs were characterized using bicinchoninic acid (BCA) assay, transmission electron microscopy (TEM), nanoparticle tracking analysis (NTA), qNano®, and flow cytometry. Protein quantification was performed using the Micro BCA™ Protein Assay Kit (Thermo Fisher, USA) following the manufacturer's instructions.[18]

The morphological characterization of EVs was performed using TEM (Tecnai G2 Spirit Biotwin, FEI, USA) equipped with a lanthanum hexaboride (LaB6) electron source and operated at an accelerating voltage of 80 kV. For imaging, a 10 μL drop of the EV suspension was placed onto carbon-coated copper grids, followed by the addition of 10 μL of 4% paraformaldehyde and incubation for one minute. The grids were subsequently washed six times with boiled and cooled ultrapure water and gently dried with a filter paper. Thereafter, 2% phosphotungstic acid was applied for one minute, washed again with ultrapure water, and dried with a filter paper (n = 6).

The particle size distribution and concentration of EVs were analyzed using the NanoSight NS300 system (Malvern PANalytical, USA) and the qNano® Gold instrument (Izon, New Zealand). For both platforms, EV samples were diluted 10-fold before loading into the respective sample chambers. Data acquisition and analysis were performed using the proprietary software provided with each instrument, enabling the determination of mean particle size and concentration as previously described.[19,20]

The phenotypic characterization of EV surface marker expression was performed using flow cytometry following an optimized bead-coupling protocol.[21] Briefly, 6 μL of carboxylated latex beads (3.5 μm diameter) were washed in PBS and centrifuged at 12 000×g to obtain a pellet. Subsequently, 2 μL of beads were incubated with 4 μL of CD63 antibody solution (Novus, NB100-77913; 1 mg mL^{-1}) for 30 minutes at room temperature (RT) and then placed on a rotator overnight at medium speed for continuous mixing. The antibody-coated beads were blocked with 5% BSA for 4 hours at RT, followed by centrifugation at 12 000×g for 10 minutes. Bead–EV conjugates were prepared by incubating 3 μg of EVs with 1 μL of the antibody-coated beads overnight on a rotator. Following incubation, the conjugates were centrifuged, pelleted, and resuspended in PBS containing 1% BSA. Secondary labeling was performed using CD81-PE antibodies, with samples incubated for 2 hours at RT. After labeling, samples were centrifuged, washed, and resuspended in PBS for analysis. Flow cytometric measurements were conducted using the Novocyte IVD system (ACEA Biosciences, Agilent, USA), and data processing was carried out with NovoExpress 1.5.0 software. Fluorophore-labeled CD81 isotype controls (Armenian hamster IgG-PE) and unstained EV samples were included to ensure accurate gating and control for nonspecific binding.

2.1.1 **Ethics approval.** All animal experiments in this study were conducted in accordance with the institutional and national guidelines for the care and use of laboratory animals. The study protocol was approved by the KOBAY DHL Inc. Local Ethics Committee (Approval No: 520, Date: 05/01/2022).

2.2. Cell uptake of extracellular vesicles

The internalization of EVs by recipient cells serves as an indicator of their biological activity and functional uptake. For the cell uptake assay, EVs were fluorescently labeled and applied to the human immortalized keratinocyte cell line (HaCaT) (RRID: CVCL_0038). Cells were seeded at a density of 10^4 cells per well in 48-well plates and incubated for 24 hours to allow attachment.

For EV labeling, SP-DiOC$_{(18)}$ (Invitrogen, USA), a lipophilic fluorescent dye, was added at a concentration of 5 μM to an EV suspension containing 10^9 particles per mL. The mixture was incubated at 37 °C for 30 minutes with intermittent vortexing to facilitate the membrane incorporation of the dye. Excess, unbound dye was removed using a 30 kDa Amicon® Ultra-2 ultrafiltration unit (Sigma Aldrich, USA). The concentrated, labeled EVs were then prepared at three different concentrations and added to the cells. After 6 hours of incubation, cells were fixed with 4% paraformaldehyde, and nuclei were counterstained with DAPI. Fluorescent images were acquired using a confocal laser scanning microscope (Zeiss, LSM800).

2.3. Dose-dependent effects of extracellular vesicles on cell proliferation

Following an injury, an adequate population of skin cells is essential to ensure proper wound coverage and maintain a healthy wound-healing process.[22] To evaluate the dose-dependent effects of EVs derived from rt-BM-MSCs on keratinocyte proliferation, experiments were conducted using the HaCaT cell line. Cells were seeded at a density of 5 × 10^3 cells per well in 96-well plates containing DMEM (4.5 g L^{-1} D-(+)-glucose; Cegrogen®, Germany) supplemented with 10% FBS, 1% L-glutamine, and 0.1% penicillin–streptomycin and incubated at 37 °C in a humidified atmosphere with 5% CO_2.

After 24 hours of attachment, cells were treated with EVs at concentrations of 0.05, 0.1, 0.25, 0.5, 1, 2.5, 5, and 10 μg mL^{-1} in a medium containing 2% FBS. Following 48 hours of incubation, cell viability was assessed using the MTT assay. The culture medium was replaced with a 10% MTT reagent (5 mg mL^{-1}) prepared in serum-free medium, and cells were incubated for 4 hours under standard culture conditions. Formazan crystals were subsequently dissolved in DMSO, and absorbance was measured at 570 nm, with background correction at 690 nm, using a spectrophotometer (Molecular Devices, USA). To account for buffer-induced variability, cells treated with an equivalent volume of the dilution buffer (without EVs) in a 2% FBS-containing medium served as the control group.

2.4. Anti-oxidative effect of extracellular vesicles

Oxidative stress, characterized by an imbalance between reactive oxygen species (ROS) production and antioxidant defense mechanisms, plays a dual role in wound healing—acting as a critical signaling mediator in processes, such as angiogenesis, while excessive ROS accumulation can induce oxidative damage, exacerbate inflammation, and ultimately delay tissue repair.[23] In this study, the protective effects of EVs on HaCaT keratinocytes subjected to oxidative stress were evaluated.

Initially, the IC$_{50}$ of H_2O_2 was determined to be 1.5 mmol (Fig. S1), which was subsequently used to induce oxidative stress in the HaCaT cells. Cells were seeded at a density of 5 × 10^3 cells per well in 96-well plates and allowed to attach for 24 hours. The culture medium was then replaced with fresh medium containing 2% FBS and EVs at concentrations of 0.25, 1, and 10 μg mL^{-1} (n = 4), followed by an additional 24 hour incubation period. To induce oxidative stress, the medium was replaced with a 1.5 mmol H_2O_2-containing medium, and cells were incubated for 4 hours. Cell viability was subsequently assessed using the MTT assay. Cells exposed solely to 1.5 mmol H_2O_2 for 4 hours served as the control group.

2.5. Preparation of the EV-integrated gelatin sponge and characterization

To prepare the EV-integrated sponges, GS was fabricated as previously described.[24] Briefly, type A gelatin (Sigma Aldrich, USA) was dissolved in distilled water to a final concentration of 4% (w/v). Glutaraldehyde (Glu; 25% v/v, Merck, Germany) was added to the gelatin solution at 0.5, 1, or 2% (v/v). The mixtures were stirred at 134×*g* for 30 minutes to induce foam formation.[25] The resulting foams were transferred into molds and frozen at −80 °C overnight. Subsequently, the frozen foams were lyophilized for 24 hours to obtain porous GS. Dried GS was cut into 1 cm × 1 cm cubes and stored at RT until characterization and further experiments. GS prepared with different glutaraldehyde concentrations were characterized by scanning electron microscopy (SEM), water-retention capacity, hydrolytic degradation, and cell-viability assays, as detailed below. The microstructural features of GS, including pore size and surface morphology, were examined by SEM (TESCAN Gaia3, Czech Republic). Prior to imaging, the GS samples were sputter-coated with gold–palladium, and images were acquired at an accelerating voltage of 30 kV and 100× magnification. To determine the swelling ratio, dry GS samples were weighed (A_0) and then immersed in distilled water for 1 hour at RT. Excess water was removed by gently tapping the samples on a filter paper, after which they were reweighed (A_1). The swelling ratio (%) was calculated using eqn (1) as follows:

$$\text{Swelling ratio}\,(\%) = \frac{A_1 - A_0}{A_0} \times 100 \tag{1}$$

The hydrolytic degradation rate of GS was assessed by quantifying gelatin protein release using the BCA assay. Cubic GS samples (1 cm × 1 cm) were first weighed (A_0) and then immersed in 5 mL of PBS, followed by incubation at 37 °C. During the first 24 hours, aliquots were collected at 3, 6, 12, and 24 hours, after which sampling was performed once daily for 4 days. At each time point, 1 mL of the degradation medium was removed and replaced with an equal volume of fresh PBS to maintain sink conditions. Gelatin concentrations in the collected samples (A_1) were determined using a BCA Protein Assay Kit (Takara, Japan) according to the manufacturer's instructions. The degradation rate was calculated as described in eqn (2) as follows:

$$\text{Degradation rate}\,(\%) = \frac{A_1}{A_0} \times 100 \tag{2}$$

The effect of GS on cell viability was evaluated using an indirect cytotoxicity assay with the mouse fibroblast cell line L-929 (NCTC clone 929; ATCC® Cat# CCL-1, RRID:CVCL_0462).[26] GS samples were prepared according to the 6 $\text{cm}^2\ \text{mL}^{-1}$ indirect cytotoxicity standard and sterilized under UV light for 45 minutes. To obtain GS extracts, the sponges were incubated in DMEM (4.5 g L^{-1} D-(+)-glucose; Sigma Aldrich, USA) supplemented with 10% FBS, 1% L-glutamine, and 0.1% penicillin–streptomycin for 72 hours at 37 °C. L-929 cells were seeded at a density of 1 × 10^4 cells per well in 96-well plates and cultured in supplemented DMEM for 24 hours at 37 °C. The culture medium was then replaced with the prepared GS extracts, and cells were incubated for an additional 24 hours under the same conditions. Cell viability was subsequently assessed using the MTT assay, as described earlier. Complete DMEM served as the negative control, while cell culture medium containing 10% DMSO was used as the positive control.

2.6. Release profile of EV-integrated gelatin sponges

For the release study, EV samples at a concentration of 10^{10} particles per mL were stained with 15 μM SP-DiOC$_{(18)}$ fluorescent dye by incubation at 37 °C for 30 min. GS samples were prepared as 6 mm diameter patches using a biopsy punch, and 60 μL of stained EV suspension was loaded into each GS patch (n = 6). The EV-loaded GS samples were placed in 2 mL PBS (pH 7.4) and then incubated at 37 °C in a shaking bath. At predetermined time intervals (0, 1, 3, 6, 12, 24, 48, and 72 h), 400 μL of the sample was withdrawn for analysis, and an equal volume of fresh PBS was added to each sample to maintain sink conditions. Before fluorescence measurement, collected samples were centrifuged at 5000×*g* for 5 min to minimize GS-related background interference. Fluorescence intensity was measured using a microplate reader (FLUOstar® Omega, Germany) at an excitation wavelength of 488 nm and an emission wavelength of 520 nm. Cumulative release profiles were expressed as percentages relative to the initial fluorescence intensity and plotted over time.

2.7. Cell migration evaluation

HaCaT cell migration is a critical component of the wound healing process, as keratinocytes must migrate into the wound bed to re-establish the epidermal barrier.[22] Keratinocyte migration not only drives re-epithelialization but also coordinates angiogenesis during the proliferative phase. To evaluate the effects of both free EVs and EV-integrated GS on keratinocyte migration, a scratch assay was performed. HaCaT cells were seeded into 24-well plates at a density of 1.5 × 10^5 cells per well and cultured for 24 hours in DMEM supplemented with 10% FBS under standard conditions (37 °C, 5% CO_2) (n = 3). The FBS concentration was then reduced to 2% to minimize proliferation, and cells were allowed to reach full confluence. A linear scratch was created using a 200 μL pipette tip, and cells were washed twice with PBS to remove detached cells. For the free EV treatment, scratched monolayers were exposed to EVs at concentrations of 0.25, 1, and 10 μg mL^{-1} in DMEM containing 2% FBS. A medium containing 2% FBS without EVs served as the control. For the EV-integrated GS treatment, cell culture inserts (pore size: 8 μm, Greiner Bio-One, Germany) were placed over the scratched monolayers, and GS samples were positioned on top of the inserts (n = 3). A total of 40 μL of EV suspension (0.25, 1, or 10 μg mL^{-1}) was pipetted onto each GS, which were allowed to absorb the EVs for 5 minutes. Subsequently, a 2% FBS-containing medium was added to both the upper and lower chambers of the insert. GS samples pre-soaked with 40 μL PBS were used as controls. Wound closure was monitored microscopically for 24 hours, and the digital images of the scratch area were captured at 0, 6, 12, and 24 hours using an inverted microscope (Leica, Germany). The quantification of wound closure was performed using the "wound_healing_size" plugin in ImageJ, which calculated the change in wound area over time.

2.8. Angiogenic potential evaluation of EV-integrated gelatin sponges

The angiogenic potentials of both free EVs and EV-integrated GS were evaluated using aortic ring and CAM assays. Because angiogenesis is essential for granulation tissue formation and wound repair,[27] these models provide physiologically relevant systems for evaluating vascular responses related to wound healing. In these experiments, EV concentrations were selected according to the biological sensitivity of the experimental models and the viability profile observed in preliminary *in vitro* assessments. Low EV doses were used in the aortic ring and CAM assays to minimize potential concentration-related adverse effects, whereas a relatively broad dose range was applied in migration and oxidative stress assays to evaluate dose-dependent cellular responses.

The aortic ring assay enables the assessment of endothelial sprouting and tube formation within an organ culture system.[28] In this study, aortas were harvested from 14 day-old chicken embryos. Fertilized eggs were obtained from the Ministry of Agriculture and Forestry Poultry Research Institute, disinfected with 20% ethanol, and incubated at 37 °C for 14 days. Following incubation, the eggs were opened, and the embryos were euthanized *via* decapitation. The thoracic cavity was exposed, and the aorta was carefully excised. Under a dissecting microscope, surrounding fat and connective tissues were removed, and the cleaned aortas were sectioned into rings of approximately 1 mm thickness.

For the experimental setup, each aortic ring was placed onto 20 μL of ECM gel (Sigma Aldrich, USA) in 48-well plates and incubated for 30 minutes at 37 °C to allow gel polymerization. GS patches (diameter: 6 mm) were loaded with EVs at concentrations of 0.5 or 5 $\mu g\ mL^{-1}$ in a 40 μL volume and positioned adjacent to the aortic rings ($n = 5$). For controls, aortic rings were also treated with free EV suspensions at identical concentrations. Cultures were maintained in 250 μL of DMEM (4.5 $g\ L^{-1}$ D-(+)-glucose) supplemented with 2.5% FBS, 1% L-glutamine, and 0.1% penicillin–streptomycin. Images were acquired on days 3 and 5 using a light microscope, and endothelial sprout length and network formation were quantified using ImageJ software.

The CAM assay provides an *in vivo*-like environment for evaluating angiogenesis. For this assay, fertilized eggs were obtained from the same facility, disinfected with 20% ethanol, and incubated at 38 °C under constant humidity (day 0). On day 3, eggs were cracked and transferred into sterile weighing boats for *ex ovo* incubation.[29] On day 7, a sterile silicone ring was placed onto the CAM surface to designate the application area. GS samples were loaded with EVs at concentrations of 0.5 or 5 $\mu g\ mL^{-1}$ and placed within the ring ($n = 5$). In parallel, 20 μL of free EVs at the same concentrations were applied directly onto the CAM twice daily ($n = 5$). The total applied EV amount was maintained equivalent between the free EV and GS-integrated groups. Embryos were incubated at 38 °C until day 9, at which point CAM images were collected for analysis. After imaging, the embryos were sacrificed by exsanguination. Vessel density was quantified using ImageJ tools, including "adjust threshold," "skeletonize," and "analyze vascular density." Quantitative data were then subjected to statistical analysis. Each CAM represented an independent biological replicate, and quantitative analyses were performed using the surviving CAM samples at the end of the experimental period.

2.9. Statistical analysis

All experiments were performed with a minimum of three biological replicates ($n \geq 3$), unless otherwise stated. Data are presented as mean ± standard deviation (SD). Student's *t*-test was performed for the dose-dependent cell viability experiment, whereas one-way ANOVA with *post hoc* pair-wise comparisons using Tukey corrections was conducted for the anti-oxidative effect analysis, cytotoxicity assessment of GS, and aortic ring and CAM assays. Two-way ANOVA with *post hoc* pair-wise comparisons using Tukey corrections was performed for the statistical analysis of the migration data. For all analyses, $p < 0.05$ was considered statistically significant, with the following notation applied: $****p < 0.0001$, $***p < 0.001$, $**p < 0.01$, $*p < 0.05$. All statistical analyses were conducted using the GraphPad Prism software (version 6.1).

3. Results and discussion

3.1. Characterization of rt-BM-MSCs-derived extracellular vesicles

EVs were successfully isolated from rt-BM-MSCs and subsequently characterized with respect to their size distribution, concentration, morphology, and phenotypic properties. Quantitative measurements obtained using qNano® and NTA demonstrated that the EVs exhibited average diameters of 163 ± 66.3 nm and 161.1 ± 60.9 nm, respectively, with corresponding particle concentrations of $4.4 \times 10^9\ mL^{-1}$ and $4.04 \times 10^9\ mL^{-1}$ (Fig. 1A and B). TEM revealed that the isolated vesicles displayed the characteristic cup-shaped EV morphology, while intact membranes indicated preserved structural integrity and biological cargo (Fig. 1C). The surface expression of EV-associated tetraspanins—particularly CD9, CD63, and CD81—which serve as established biomarkers for EV identification, was assessed.[30] In this study, CD81 expression was assessed by flow cytometry, and the analysis confirmed the presence of CD81 on the vesicle surfaces (Fig. 1D). Collectively, these results verified that the isolated particles possessed the expected morphological and phenotypic features of MSC-derived EVs within a defined size range (50–200 nm), supporting their suitability for subsequent experimental applications.[7]

3.2. Dose-dependent cell uptake of extracellular vesicles

The cellular uptake capacity of EVs was assessed in a dose-dependent manner, with concentrations ranging from 10^7 to 10^9 particles mL^{-1}. EV dosing in a cell uptake experiment was based on particle concentration rather than protein amount, enabling a precise control over the particle-to-cell ratio. As shown in Fig. 2, green-labelled EVs were observed predominantly around the cytoplasmic region, indicating successful

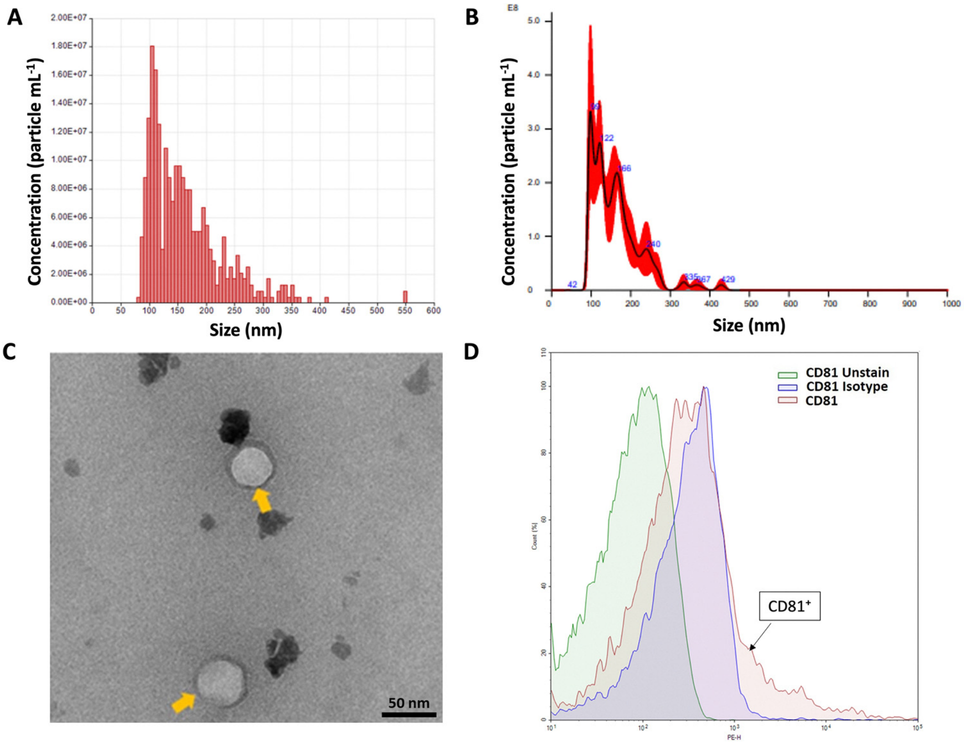

Fig. 1 Characterization of the rt-BM-MSC-derived EVs. (A) qNano® analysis showing the mean particle diameter and concentration of the EVs. (B) NTA demonstrating the mean particle diameter and concentration of the EVs. (C) Representative TEM images of the rt-BM-MSC-derived EVs (scale bar: 50 nm, yellow arrows: EVs). (D) Flow cytometric analysis of the CD81 expression of the rt-BM-MSC-derived EVs.

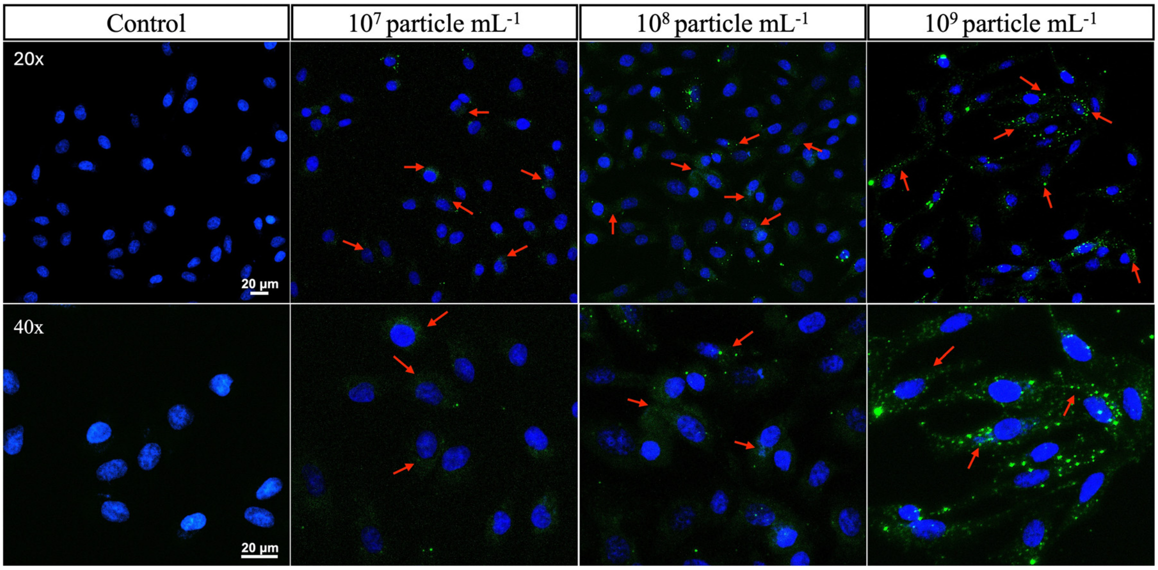

Fig. 2 Representative confocal images showing the cellular uptake of EVs in the HaCaT cells (scale bar: 20 μm, the cell nuclei stained blue, and the SP-DiOC$_{(18)}$-labeled EVs appearing green at varying concentrations marked with red arrows).

and specific internalization. In all tested concentrations, EVs were taken up by the cells within 6 hours; however, the extent of uptake increased markedly with increased EV concentrations, demonstrating a clear dose-dependent internalization profile.

3.3. Effects of extracellular vesicles on cell proliferation, oxidative stress and migration response

The HaCaT cells were treated with increasing concentrations of EVs to investigate the proliferative effects of rt-BM-MSC–derived EVs on keratinocytes, and cell viability was assessed after 48 hours using the MTT assay. As shown in Fig. 3A, EV treatment affected HaCaT cell viability in a dose-dependent manner. At concentrations below 2.5 μg mL^{-1}, EVs did not significantly alter cell viability relative to the control group; only the 0.25 μg mL^{-1} group showed an increase in cell viability (111%); however, this difference was not statistically significant ($p > 0.05$). The reduction observed in cell viability with increasing EV concentration may be attributed to the enriched molecular cargo of these EVs, which could potentially influence cell-cycle dynamics; however, this hypothesis requires further investigation. Similar dose-dependent decreases in cell viability have been reported in NIH/3T3 fibroblasts exposed to increasing concentrations of MSC-derived EVs,[31] and similar findings have been noted for the HaCaT cells, with reduced *in vitro* efficacy at high EV concentrations.[32]

For antioxidant capacity evaluation, a relatively narrow concentration range was selected on the basis of cell viability results. The HaCaT cells were pre-treated with EVs prior to the induction of oxidative stress using H_2O_2. As shown in Fig. 3B, EVs exhibited a dose-dependent protective effect and mitigated H_2O_2-induced cytotoxicity after 24 hours. The 0.25 μg mL^{-1} EV group displayed the highest protective response, with cell viability increasing to 112.5% compared to the H_2O_2 control ($p < 0.05$). No significant difference was observed between the 0.25 and 1 μg mL^{-1} groups ($p > 0.05$). Similar to cell viability, increasing the dose from 0.25 to 10 μg mL^{-1} resulted in a decrease from 112.5% to 67.7% ($p < 0.05$). A reduction was also observed between the 10-μg mL^{-1} group and H_2O_2 control ($p < 0.001$) group. Oxidative stress plays a central role in the pathogenesis of numerous conditions by influencing ROS scavenging, inflammatory signaling, apoptosis, and vascular repair mechanisms. Several studies have demonstrated the protective effects of EVs against oxidative damage. Wang *et al.* reported that MSC-derived exosomes markedly attenuated oxidative responses in H_2O_2-treated keratinocytes.[33] Similarly, Lin *et al.* showed that UC-MSC-derived EVs exerted a dose-dependent antioxidant effect in H_2O_2-exposed HaCaT cells, with increasing particle numbers enhancing the protective response.[34] The present study demonstrated that EVs show a protective effect against oxidative stress in a dose-dependent manner. A possible explanation for this phenomenon is provided by a comprehensive study conducted by Hagey *et al.*, who examined the cellular responses and transcriptional profiles of fibroblasts treated with EVs derived from various cellular sources. Their findings revealed that low EV doses (approximately 20 particles per cell) elicited distinct transcriptional signatures and strong surface-protein–mediated signaling in a cell-specific manner.[35] This work highlights that the optimal functional dose of EVs is highly dependent on both the biological process being evaluated and the cellular origin of the vesicles. When considered alongside these insights, the difference between our results and previously reported findings may be related to EV source, concentration, and the dose–response characteristics.

The migration response of the HaCaT cells to free EVs was evaluated using a scratch assay. The HaCaT cells were treated with EVs at the same concentration range as that for the oxidative stress assays. The results are given in Fig. 3C and D. Fig. 3C presents representative scratch assay images of the control and EV-treated groups (0.25, 1, and 10 μg mL^{-1}) at 0, 6, 12, and 24 h. Progressive wound closure was observed over time in all groups. Fig. 3D quantitatively presents the time-dependent changes in the wound area for the control and EV-treated groups. In all groups, the wound area gradually decreased from 0 to 24 h, indicating progressive wound closure over time. The remaining wound area in the control group was 49.65% ($p < 0.0001$) relative to the initial wound area after 24 hours. In the EV-treated groups, the corresponding remaining wound areas were higher than in the control group, with values of 62.02% ($p < 0.0001$), 76.99% ($p < 0.0001$), and 71.99% ($p < 0.0001$) relative to the initial wound area after 24 hours for the 0.25, 1, and 10 μg mL^{-1} EV concentrations, respectively.

3.4. Gelatin sponges are feasible carriers for extracellular vesicles

GS samples were prepared for use as carriers for EVs in this study. The freeze-dried GS samples exhibited a white, porous, soft, and flexible structure (Fig. 4A), characteristics that facilitate their ability to conform easily to irregular wound surfaces. The cytocompatibility of GS was further assessed using L-929 fibroblasts. As shown in Fig. 4B, none of the GS formulations demonstrated cytotoxic effects. The non-cross-linked GS group, used as the negative control, exhibited 98.97% cell viability, whereas the positive control group displayed 20% viability. The GS-Glu groups showed viabilities of 92.50%, 93.99%, and 96.98% ($p < 0.0001$) at increasing glutaraldehyde concentrations; all exceeded the 70% viability threshold, which indicated non-cytotoxicity and was significantly higher than that of the positive control group. SEM revealed an average pore diameter of approximately 200 ± 50 μm (Fig. 4C). Notably, the pore morphology remained similar across all glutaraldehyde cross-linking concentrations, as expected; differences between groups were expected to emerge primarily in processes involving chemical bond–dependent behaviors, such as degradation. The time-dependent hydrolytic degradation of glutaraldehyde-cross-linked GS was evaluated using BCA analysis. GS-2% Glu exhibited the highest retention capacity, with 77.91% degradation by day 4. In contrast, GS-1% Glu underwent complete degradation by day 1, while GS-0.5% Glu and non-cross-linked GS showed relatively fast degradation profiles, with complete degradation occurring within 6 h and 3 h, respectively (Fig. 4D). The water-retention capacities of the glutaraldehyde cross-linked GS ranged from 3380% to 4504%, a favorable characteristic for absorbing wound exudate (Table 1). Based on the combined degradation profiles and biocompatibility outcomes, GS-2% Glu was selected as the EV carrier. Following the selection, EV-loaded GS-2% Glu scaffolds were evaluated for their release behavior and biological activity in subsequent functional assays. As shown in Fig. 4E, EV release gradually increased over time. At the end of 6 h, the EV release from GS was 13.8%, and it reached 86.0% at 72 h. EV loading onto GS provided a controlled release, thereby eliminating the effects associated with a high initial dose. Due to the hydrophilic nature of gelatin, both bulk and surface erosion are known to occur.[25]

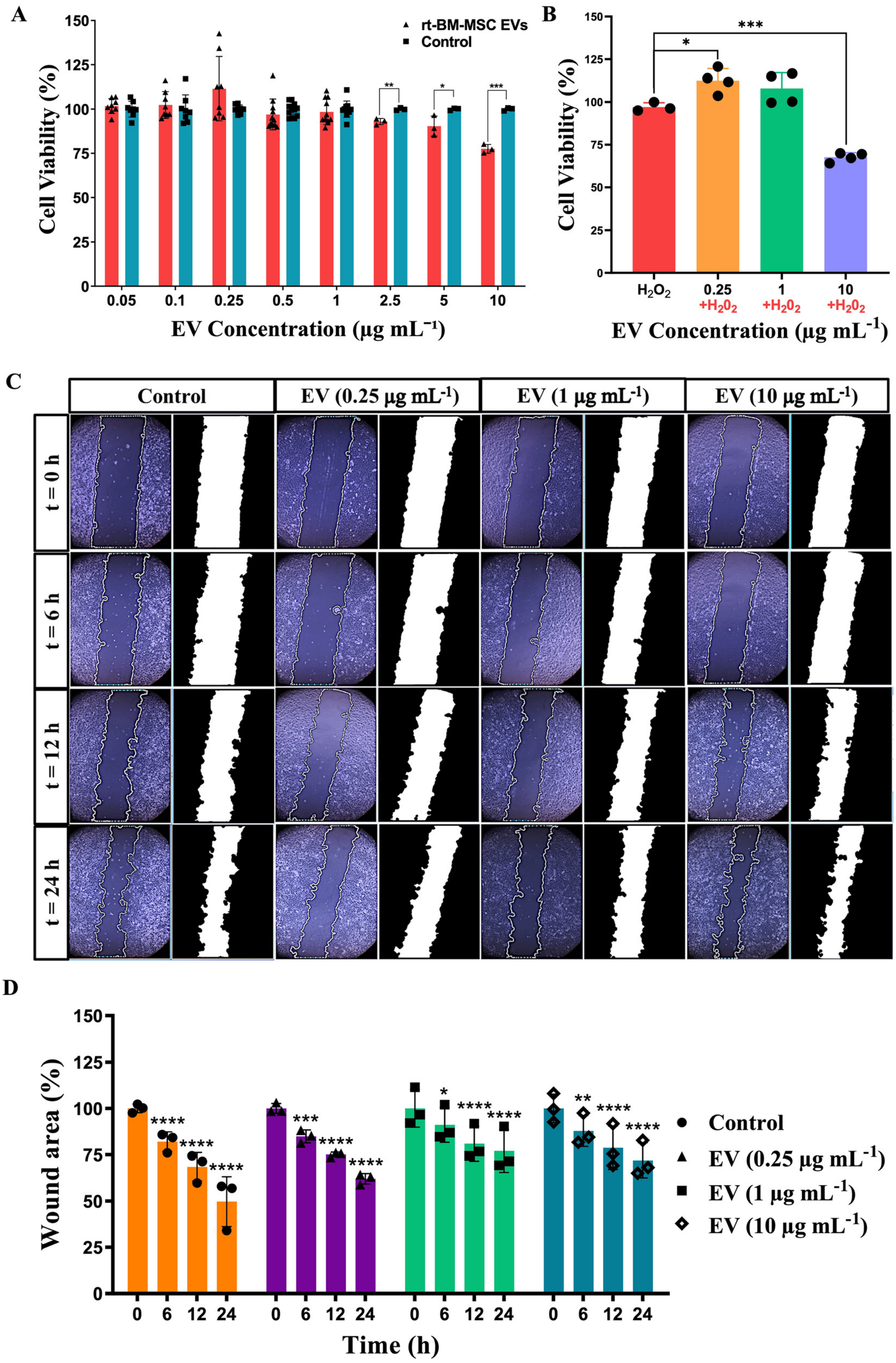

Fig. 3 Proliferation and antioxidative effects of the EVs on the HaCaT cells. (A) HaCaT cell viability after 48 hours of treatment with varying concentrations of EVs. Each treatment group was statistically compared with its corresponding control group. (B) Antioxidative effects of the EVs on the HaCaT cells at different EV concentrations. (C) Representative images from the EV-treated HaCaT cell migration assay. (D) Quantitative analysis of the wound closure at 0, 6, 12, and 24 hours. Asterisks indicate the statistical significance between the initial (0 h) wound area and the defined time intervals (6, 12, or 24 h). ****$p < 0.0001$, ***$p < 0.001$, **$p < 0.01$, and *$p < 0.05$ (two-way ANOVA and Tukey multiple comparison).

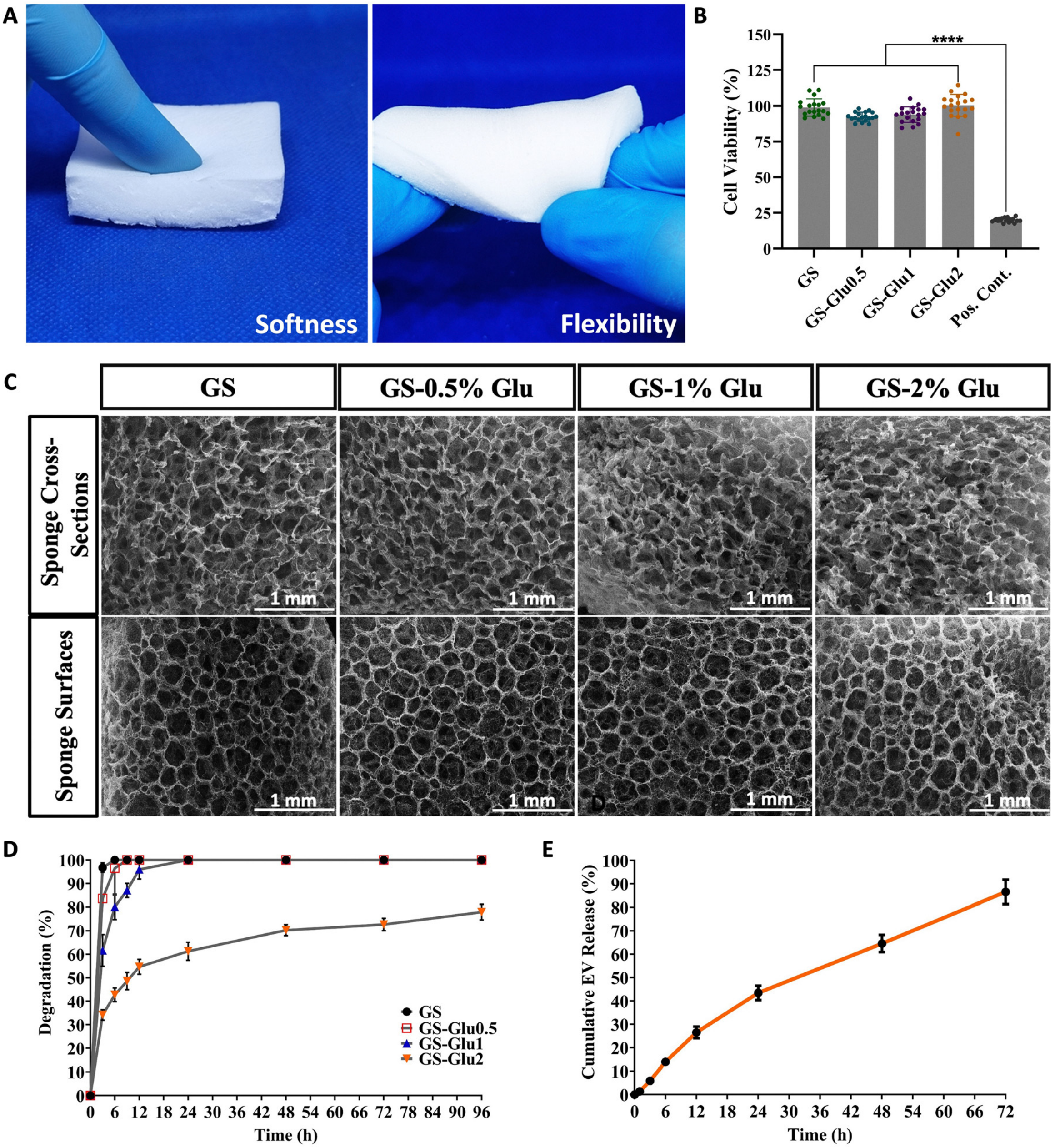

Fig. 4 Characterization of the GS cross-linked with different glutaraldehyde concentrations and evaluation of the EV release profile. (A) Macroscopic images illustrating the soft and flexible structure of the GS. (B) Cytotoxicity assessment of the GS in L-929 fibroblasts (Pos. Cont.: 10% DMSO). (C) SEM micrographs showing the microstructure of the GS from both inner and outer surfaces. (D) Hydrolytic degradation profiles of the GS, determined by the BCA analysis. (E) Sustained release profile of the EVs from the GS in PBS (pH 7.4) at 37 °C over 72 h. The geometric symbols represent individual data points. ****$p < 0.0001$ (one-way ANOVA and Tukey multiple comparison).

Table 1 Water retention capacity of GS

Group	Water retention capacity (%)
GS	4504
GS-Glu0.5	4446
GS-Glu1	4305
GS-Glu2	3380

Therefore, EV release is thought to occur through both diffusion and erosion. The degradation profile of EV-loaded GS also supported this behavior. The incorporation of EVs onto GS without compromising their biological activity was a critical objective of this study. A previous study confirmed the importance of the delivery systems *via* single-particle tracking analysis. The results demonstrated that free EVs were prone to membrane disruption and aggregation due to continuous displacement, whereas embedding EVs within GelMA significantly enhanced their structural stability and preserved their functional properties.[36] Similarly, adipose-derived stem cell EVs released from commercial gelatin sponges in a controlled manner over one week were shown to markedly improve bone regeneration in both *in vitro* and *in vivo* models.[37] In another study, commercial gelatin sponges loaded with human umbilical-cord MSC-derived EVs exhibited strong hemostatic activity across *in vitro* and *in vivo* models.[38] These findings supported the feasibility of developing a GS-based delivery system for maintaining EV structural stability and preserving bioactivity. Here, we offer GS scaffolds for EV delivery with an optimized and simple protocol.

3.5. Extracellular vesicles-integrated gelatin sponges alleviate cell migration

Cell migration is a critical process of wound healing, during which keratinocytes and other healthy cells migrate from the wound edges toward the center to restore epidermal continuity. The migration response of the HaCaT cells to EV-integrated GS was evaluated using the scratch assay. The GS-related results are given in Fig. 5. Fig. 5A presents the representative scratch assay images of the GS control and EV-GS-treated groups (0.25, 1, and 10 μg mL^{-1}) at 0, 6, 12, and 24 h. Progressive wound closure was observed over time in all groups. Fig. 5B shows the quantitative analysis of wound closure. The remaining wound area in the GS control was 30.29% ($p < 0.0001$) after 24 hours, relative to the initial wound area. In the EV-integrated GS groups, the corresponding remaining wound areas were 27.06% ($p < 0.0001$), 27.28% ($p < 0.0001$), and 35.42% ($p < 0.0001$) for 0.25, 1, and 10 μg mL^{-1} concentrations, respectively.

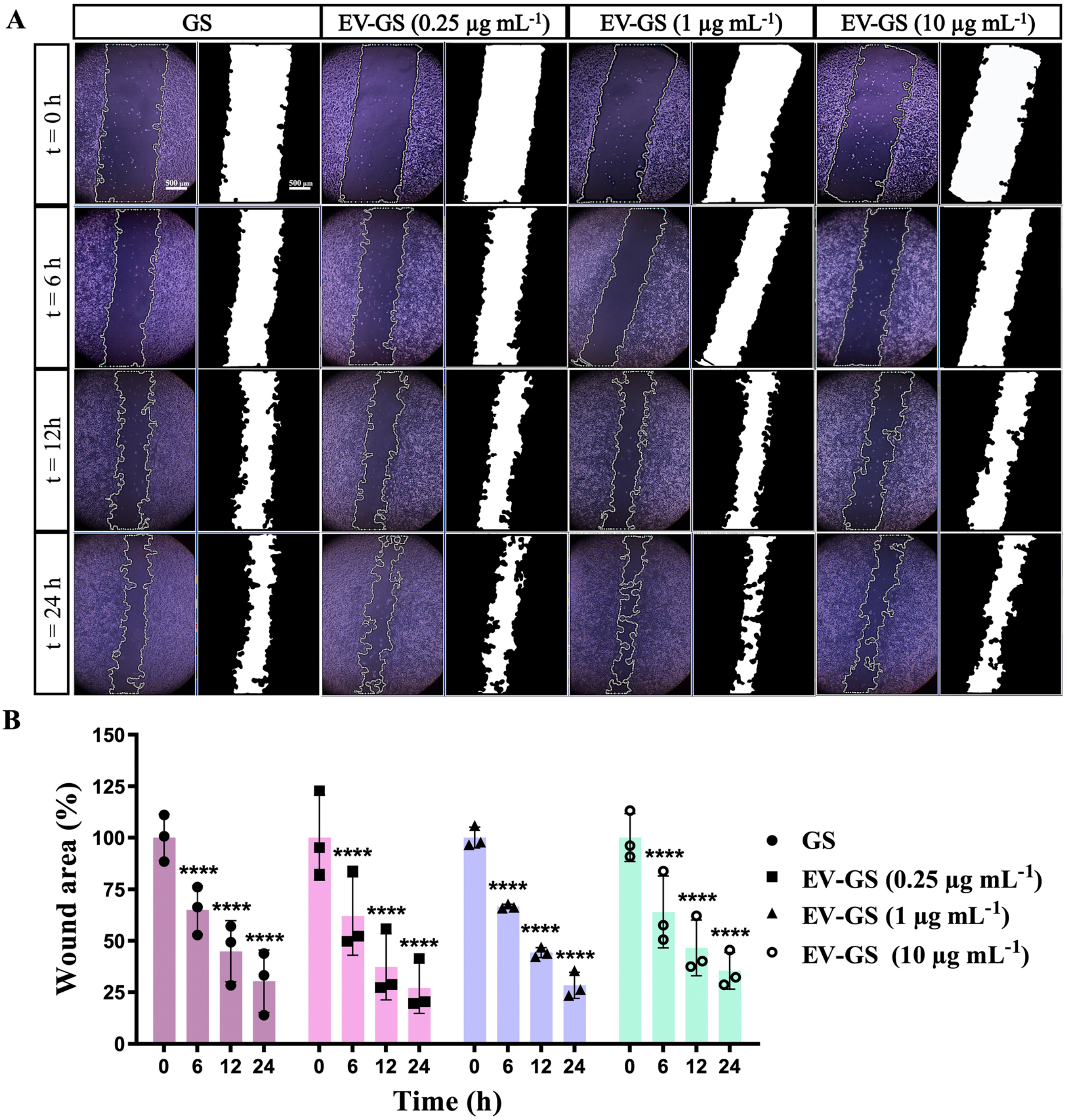

Fig. 5 (A) Migration activity of the HaCaT cells over a 24 hour period following treatment with the EV-integrated GS ($n = 3$). (B) Quantitative analysis of the wound closure at specified time points. Asterisks indicate the statistical significance between the initial (0 h) wound area and the defined time intervals (6, 12, or 24 h). ****$p < 0.0001$ (two-way ANOVA and Tukey multiple comparison).

EVs have been shown to influence the migration capacity of both fibroblasts and keratinocytes through the regulatory actions of miRNAs and various signaling pathways.[39,40] Ferreira *et al.* reported significantly enhanced keratinocyte migration following treatment with adipose-derived MSC-EVs, even at relatively low EV concentrations (3.67×10^7 mL^{-1}). Notably, their study did not include comparisons across multiple EV doses.[41] In our work, the incorporation of EVs into GS enhanced wound closure rates compared to free EVs, with a substantial decrease in wound area occurring in the 0.25 μg mL^{-1} EV-integrated GS group (27.06%). Therefore, the improved wound closure highlighted the potential of the EV-integrated GS to support the epithelial repair phase of wound healing. Our findings also aligned with those of Wang *et al.*, who demonstrated that loading 1 μg of EVs into 100 μL of hydrogel significantly increased HUVEC migration compared to both control and free-EV groups.[42] These results were consistent with our previous findings, suggesting that EVs had dose-dependent effects on cell migration, with low-dose EV treatments---particularly when delivered *via* a carrier system—providing the greatest benefit. Collectively, the enhanced migration observed with EV-integrated GS indicated that this platform facilitated early epithelial repair and complemented its pro-angiogenic effects.

3.6. Extracellular vesicle-integrated gelatin sponges promote angiogenesis

A substantial body of research has demonstrated that stem-cell-derived EVs play a pivotal role in angiogenesis. These vesicles transport proteins, nucleic acids, and other bioactive molecules capable of activating angiogenesis-specific signaling pathways, as documented in numerous studies.[43,44] Although *in vitro* tube formation assays are widely used to assess endothelial

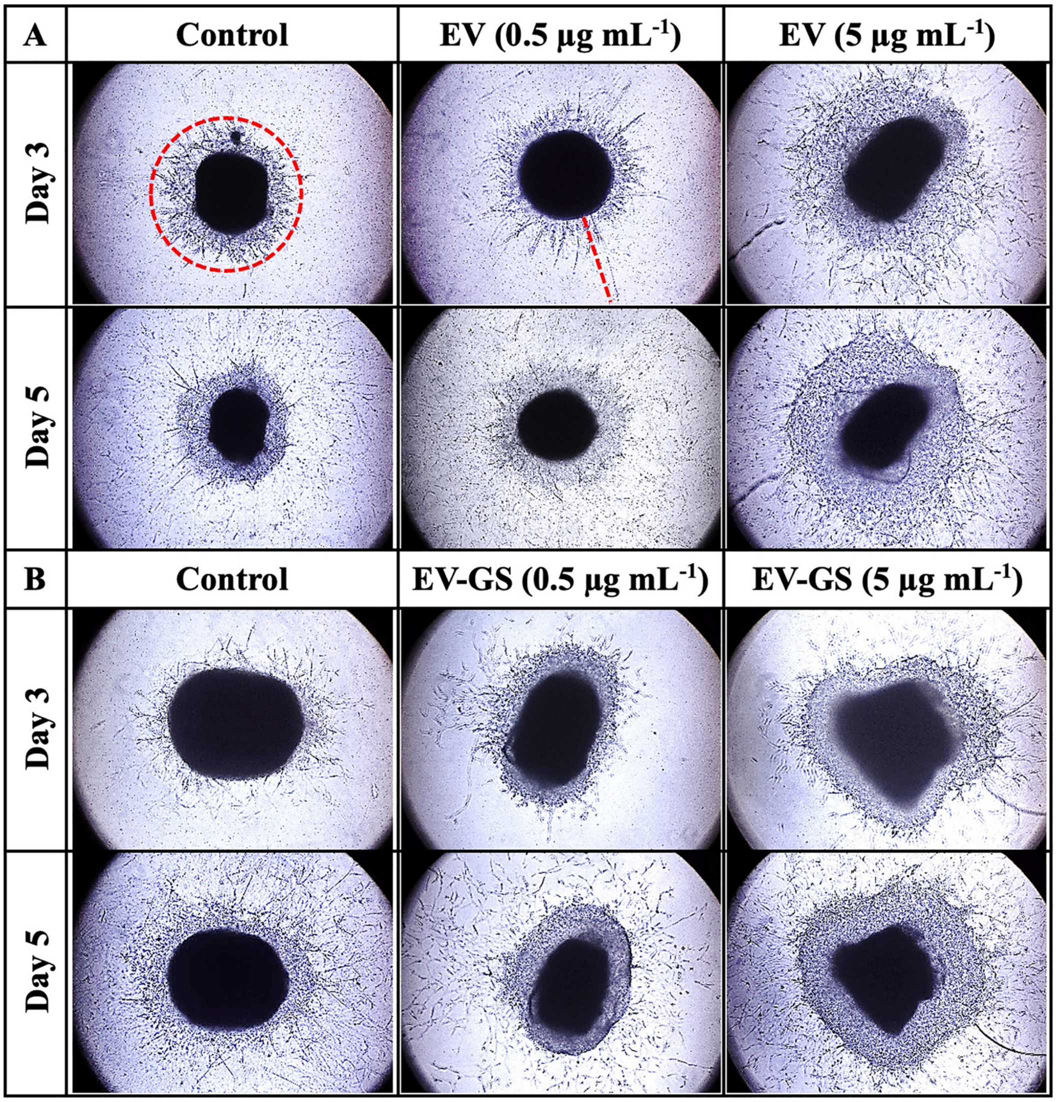

Fig. 6 Angiogenic effect of the EV suspension and EV-integrated GS in the aortic ring assay. (A) Representative images of the aortic rings treated with the free EV suspensions on days 3 and 5. (B) Representative images of the aortic rings treated with the EV-integrated GS on days 3 and 5 (scale bar = 1000 μm, red circles indicating the endothelial sprout networks, and red lines denoting the individual endothelial sprouts).

angiogenic activity, angiogenesis is inherently a multicellular and microenvironment-dependent process. Therefore, more complex assay systems are needed to better capture the physiological context. In this regard, the aortic ring and the CAM assays represent valuable alternatives, as they preserve multicellular interactions and extracellular matrix components essential for angiogenic progression. The use of different EV concentrations across assays was based on assay-specific biological sensitivity. Since high EV concentrations showed a tendency to reduce cell viability, low doses were preferred in the aortic ring and CAM models, which were more sensitive and physiologically complex angiogenesis systems. This dose-adjusted approach enabled the evaluation of EV-mediated angiogenic responses while minimizing potential concentration-related adverse effects.

The *ex vivo* aortic ring assay was employed to assess the angiogenic effects of both free EVs and EV-integrated GS on endothelial cells in an organ culture system. Aortic rings were cultured for 5 days and imaged on days 3 and 5. Based on our previous optimization studies, a 5 day incubation period was determined to be optimal for chick aortic rings, as endothelial cell viability began to decline beyond this timeframe. As shown in Fig. 6, endothelial cells maintained their viability throughout the culture period, displaying homogeneous proliferation and migration along the aortic ring walls. EV-integrated GS (Fig. 6B) elicited angiogenic responses comparable to those observed with free EVs (Fig. 6A).

The quantitative analysis of endothelial sprouting and network formation is presented in Fig. 7. In the free EV groups, endothelial sprout length on day 5 was significantly greater at the 5 μg mL^{-1} dose (918.14 ± 290.105 μm, $p < 0.01$) compared to the 0.5 μg mL^{-1} dose (370.535 ± 102.464 μm) (Fig. 7A). Similarly, in the EV-integrated GS groups, sprout length on day 3 was higher at 5 μg mL^{-1} (637.958 ± 138.269 μm, $p < 0.05$) than at 0.5 μg mL^{-1} (321.007 ± 42.80 μm) and the GS control (Fig. 7C). Endothelial network formation for free EVs at days 3 and 5 (Fig. 7B and D) was similar ($p > 0.05$); however, it was significantly higher in the 5 μg mL^{-1} EV-integrated GS group compared to the 0.5 μg mL^{-1} dose at day 3 ($p < 0.05$). Across all experimental groups, endothelial cells retained their viability and proliferation ability following treatment with free EVs or EV-integrated GS. The earlier observation of concentration-dependent differences in the GS groups suggested that EVs were protected from degradation, and their bioactivity was maintained within the GS. Hao *et al.* reported enhanced endothelial activity of human placental MSC-derived EVs in rat aortic rings following seven days of treatment.[45] Johnson *et al.* provided a more comprehensive analysis by comparing the angiogenic potential of EVs derived from different cellular sources using a mouse aortic ring assay. Their findings revealed significant differences at the 10 μg mL^{-1} EV concentration, underscoring the dose- and source-dependent characteristics of EV-mediated angiogenesis,[46] similar to other biological

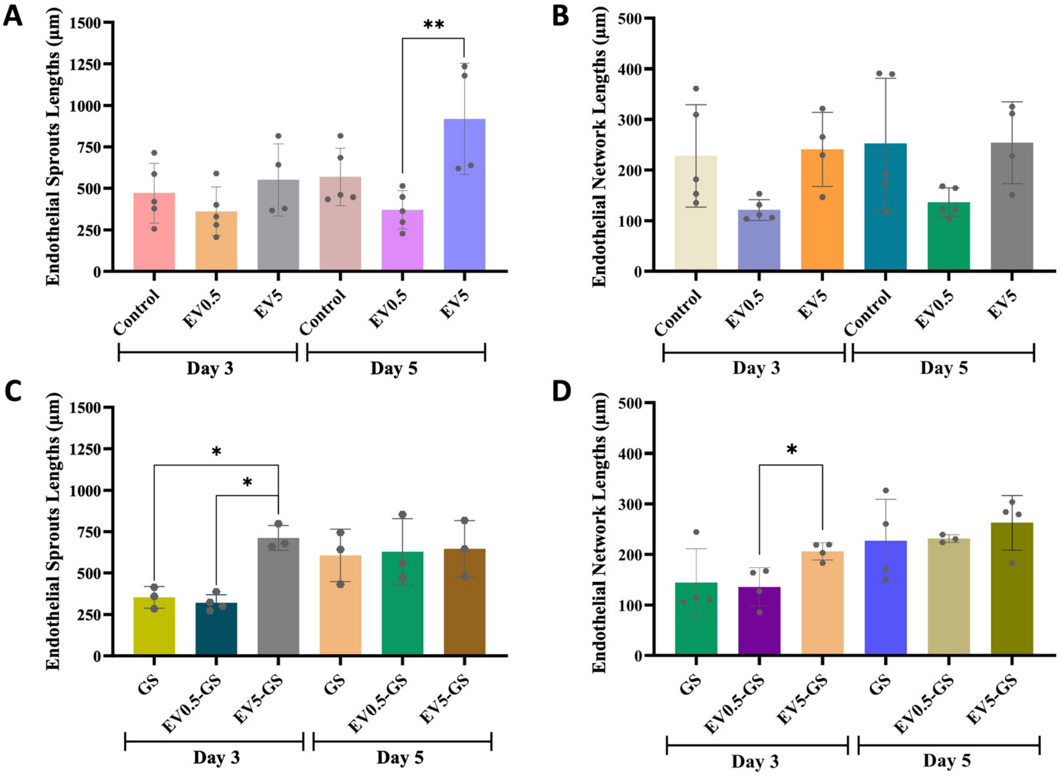

Fig. 7 Quantitative analysis of the endothelial sprout and network formation on days 3 and 5. (A) Endothelial sprout lengths measured in the aortic rings treated with the free EVs. (B) Endothelial network lengths formed in response to the free EV treatment. (C) Endothelial sprout lengths in the aortic rings exposed to the EV-integrated GS. (D) Endothelial network lengths observed following treatment with the EV-integrated GS. **$p < 0.01$ and *$p < 0.05$ (one-way ANOVA and Tukey multiple comparison).

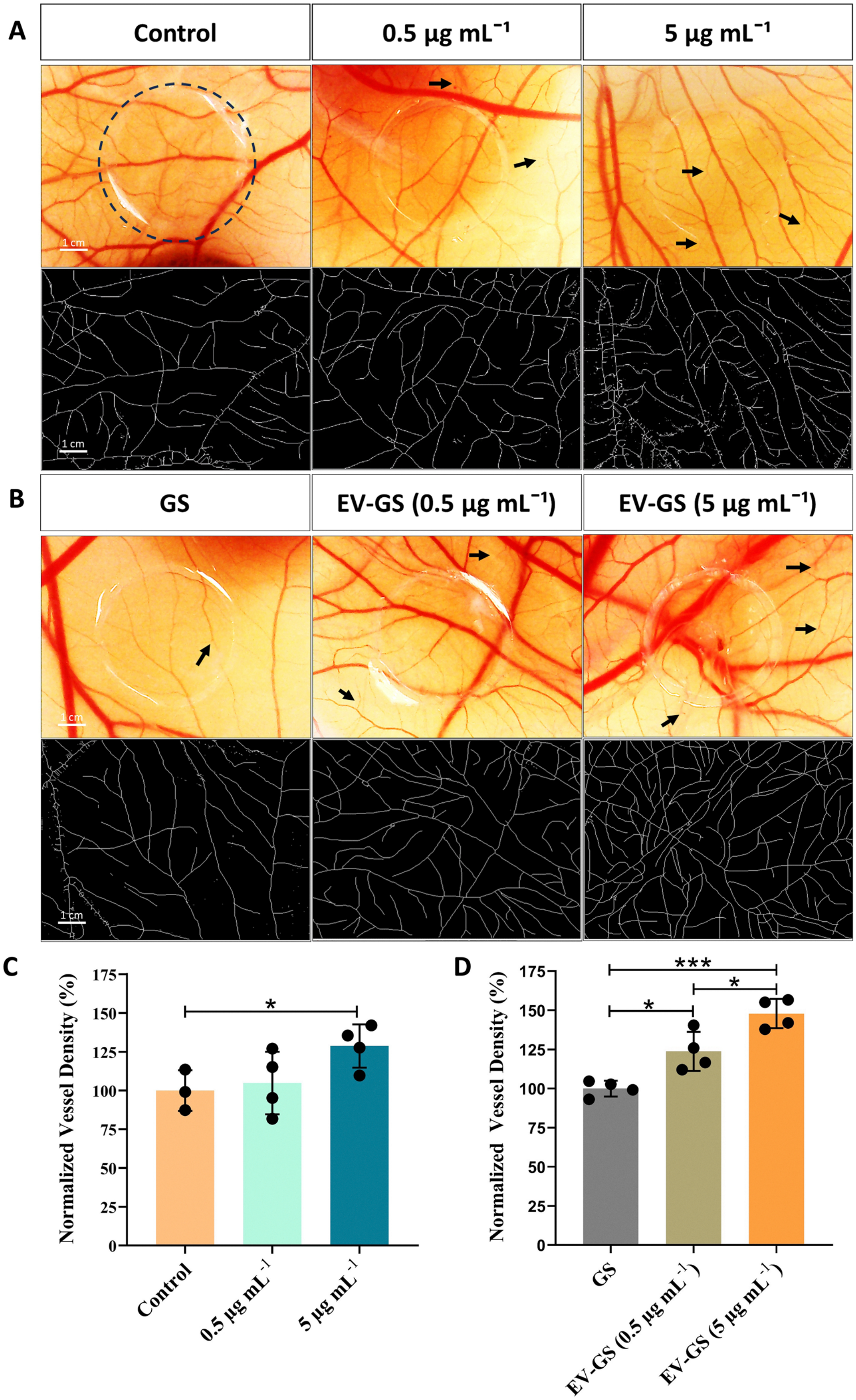

Fig. 8 Angiogenic effects of the free EVs and EV-integrated GS in the *ex ovo* CAM assay. (A) Macroscopic and skeletonized images of the CAMs treated with the free EVs. (B) Macroscopic and skeletonized images of the CAMs treated with the EV-integrated GS. (C) Quantitative analyses derived from the skeletonized images of the CAMs treated with the free EVs. (D) Quantitative analyses derived from the skeletonized images of the CAMs treated with the EV-integrated GS (black arrows indicating the newly formed vascular branches; the dashed circle denoting the O-ring positioned on the CAM). ***$p < 0.001$ and *$p < 0.05$ (one-way ANOVA and Tukey multiple comparison).

processes. Our study introduced the use of the chicken embryo aortic ring assay for evaluating EV-integrated GS for the first time and demonstrated the feasibility of using a carrier system within this model. The GS-based delivery approach was also innovative in the context of the aortic ring assay, offering prolonged EV retention.

The CAM assay was employed to investigate angiogenesis, offering a more complex and physiologically relevant system than conventional *in vitro* cell-based models. The use of gelatin GS as scaffolds on the CAM assay was first introduced in 1997, demonstrating that bioactive molecules applied to the CAM remained localized for extended periods, thereby increasing the reliability and sensitivity of angiogenic assessments.[47] Here, *ex ovo* chick embryo CAM assay was employed to evaluate the angiogenic effects of free EVs and EV-integrated GS. Based on the cell viability findings, EV concentrations of 0.5 and 5 $\mu g\ mL^{-1}$ were selected for loading onto GS. At these concentrations, both free EVs and EV-integrated GS applied to the CAM and angiogenesis were assessed on day 9, revealing a concentration-dependent increase in vessel density in each treatment group. As anticipated, GS alone exhibited no signs of toxicity on the CAM.

Fig. 8A shows representative CAM images and corresponding vessel skeletonization analyses following treatment with free EVs at 0.5 and 5 $\mu g\ mL^{-1}$ concentrations. Compared with the untreated control group, free EV increased vascular sprouts and vessel density in a dose-dependent manner, as indicated by the relatively dense vascular network observed in the processed skeletonized images. Fig. 8C quantitatively confirmed this observation. Free EVs increased normalized vessel density by approximately 10% at 0.5 $\mu g\ mL^{-1}$ and by 30% ($p < 0.05$) at 5 $\mu g\ mL^{-1}$, compared with the control group. Fig. 8B presents CAM images of the GS control and EV-integrated GS groups. The EV-integrated GS samples increased vessel formation toward and around the implanted material compared to the GS control. This effect was particularly evident in the EV-GS 5 $\mu g\ mL^{-1}$ group, where a dense and widespread vascular network was observed. Fig. 8D further supported these observations quantitatively. Compared with the GS control, EV-integrated GS increased normalized vessel density by approximately 25% ($p < 0.05$) at 0.5 $\mu g\ mL^{-1}$ and by nearly 50% ($p < 0.001$) at 5 $\mu g\ mL^{-1}$. Overall, these findings demonstrated that EV incorporation into GS preserved and potentiated the pro-angiogenic activity of EVs in the CAM model. Notably, approximately 86% of EV release was achieved within 72 h, corresponding to the duration of EV administration used in the angiogenesis assays. This sustained release profile may have contributed to the enhanced angiogenic response observed in the EV-integrated GS groups. Compared with free EVs and GS alone, EV-integrated GS exhibited superior angiogenic efficacy, suggesting that the porous GS structure supported localized EV retention and spatial confinement, thereby promoting more sustained EV–cell interactions and improving signaling efficiency. Collectively, these results indicated that GS functioned not merely as a passive carrier but as a supportive delivery matrix actively controlling the EV release profile. Previous studies also presented different results about the angiogenic potential of EVs in the CAM assay. While Ma *et al.* showed enhanced new vessel formation due to Akt-modified hUC-MSC-derived EVs *in ovo* CAM assay,[48] Merckx *et al.* observed no significant difference with the evaluated BM-MSC-derived EV treatment within Matrigel®.[49] The experimental parameters used in our CAM assay—including EV source, dosing strategy, application methodology, and the utilization of GS as a carrier—differed from those employed in previous investigations, which may result in the observed variability in angiogenic outcomes. The combined results from both the aortic ring and CAM assays consistently demonstrated the efficacy of EV-integrated GS in promoting angiogenesis.

Moreover, throughout the experimental period, most of the embryos remained viable, and no pathological alterations—such as infection or hemorrhage—were observed in any of the groups treated with free EVs or EV-integrated GS. Additionally, these experiments confirmed that EV-integrated GS were non-toxic, posing no adverse effects on embryonic development or organ culture systems. These safety observations aligned with previously published data on EV-based and gelatin-based biomaterials.[25,38] The GSs used in this study were fabricated *via* 2% glutaraldehyde crosslinking, followed by lyophilization and comprehensive characterization for porous architecture, hydrolytic degradation behavior, water-retention capacity, and cytocompatibility. The gentle fabrication process enabled precise control over the physical properties of the sponges. Their interconnected, highly porous structure provided an optimal microenvironment for angiogenesis—a process that was tightly coordinated with earlier wound healing events, such as cell proliferation and migration. The successful integration of EVs onto GS and the resulting enhancement in angiogenesis indicated that the biological activity of EVs was effectively preserved within the scaffold and that a sustained release profile was achieved through gradual GS degradation. Furthermore, the study highlighted that EVs exerted distinct biological effects, depending on the specific cellular or molecular context, as reflected in the differing responses observed across proliferation and migration assays at varying EV concentrations. While this study did not include a full-thickness cutaneous wound model, the integration of biomaterial-based EV delivery with two complementary angiogenesis platforms yielded robust mechanistic evidence about the wound healing biology. As impaired angiogenesis is a primary contributor to chronic non-healing wounds, the observed pro-angiogenic activity supports the potential of this platform for application in future *in vivo* wound models and clinical translation.

4. Conclusion

This study demonstrated that GS could serve as a biocompatible, biodegradable, and clinically accessible platform for the local delivery of rt-BM-MSC-derived EVs. *In vitro* analyses showed that EV-mediated effects on wound healing-related cellular responses were dose-dependent, emphasizing the complexity of EV bioactivity and the need for further mechanistic investigation. In addition, scratch assays demonstrated improved cell migration, while aortic ring and CAM assays revealed enhanced angiogenic responses in the EV-integrated GS groups, compared with those for free EV treatment. These findings suggested that GS not only provided a suitable delivery matrix for EVs but may also improve their therapeutic performance in wound healing-related environments. Overall, EV-integrated GS represents a portable and locally applicable biomaterial platform with translational potential, particularly for chronic wounds characterized by impaired angiogenesis. Our next plan is to demonstrate the potential of the developed EV-integrated GS in wound healing by proving its biological activities in an *in vivo* model.

Author contributions

CRediT: Elif Conger-Onder: formal analysis, investigation, methodology, validation, visualization, writing – original draft. Sukru Ozturk: formal analysis, methodology, writing – review and editing. Naside Mangir: methodology, writing – review and editing. Alp Can: funding acquisition, writing – review and editing. Kezban Ulubayram: conceptualization, funding acquisition, methodology, project administration, resources, supervision, writing – review and editing.

Conflicts of interest

There are no conflicts to declare.

Data availability

All data accessed or analyzed in this study are available in the article.

Supplementary information (SI) is available. See DOI: https://doi.org/10.1039/d6tb00705h.

Acknowledgements

This study was supported by The Scientific and Technological Research Council of Türkiye, grant number 120S910, and partly by the Ankara University Scientific Research Fund (TSG-2020–2545 to AC).

References

1 C. K. Sen, *Adv. Wound Care*, 2021, **10**, 281–292.
2 D. Chouhan, N. Dey, N. Bhardwaj and B. B. Mandal, *Biomaterials*, 2019, **216**, 119267.
3 B. M. Borena, A. Martens, S. Y. Broeckx, E. Meyer, K. Chiers, L. Duchateau and J. H. Spaas, *Cell. Physiol. Biochem.*, 2015, **36**, 1–23.
4 D. S. Baranovskii, I. D. Klabukov, N. V. Arguchinskaya, A. O. Yakimova, A. A. Kisel, E. M. Yatsenko, S. A. Ivanov, P. V. Shegay and A. D. Kaprin, *Stem Cell Investig.*, 2022, **9**, 7.
5 K. E. Johnson and T. A. Wilgus, *Adv. Wound Care*, 2014, **3**, 647–661.
6 T. Cui, R. S. Kirsner and J. Li, *Adv. Wound Care*, 2010, **1**, 347–352.
7 J. A. Welsh, D. C. I. Goberdhan, L. O'Driscoll, E. I. Buzas, C. Blenkiron, B. Bussolati, H. Cai, D. Di Vizio, T. A. P. Driedonks, U. Erdbrügger, J. M. Falcon-Perez, Q. L. Fu, A. F. Hill, M. Lenassi, S. K. Lim, M. G. Mahoney, S. Mohanty, A. Möller, R. Nieuwland, T. Ochiya, S. Sahoo, A. C. Torrecilhas, L. Zheng, A. Zijlstra, S. Abuelreich, R. Bagabas, P. Bergese, E. M. Bridges, M. Brucale, D. Burger, R. P. Carney, E. Cocucci, R. Crescitelli, E. Hanser, A. L. Harris, N. J. Haughey, A. Hendrix, A. R. Ivanov, T. Jovanovic-Talisman, N. A. Kruh-Garcia, V. Ku'ulei-Lyn Faustino, D. Kyburz, C. Lässer, K. M. Lennon, J. Lötvall, A. L. Maddox, E. S. Martens-Uzunova, R. R. Mizenko, L. A. Newman, A. Ridolfi, E. Rohde, T. Rojalin, A. Rowland, A. Saftics, U. S. Sandau, J. A. Saugstad, F. Shekari, S. Swift, D. Ter-Ovanesyan, J. P. Tosar, Z. Useckaite, F. Valle, Z. Varga, E. van der Pol, M. J. C. van Herwijnen, M. H. M. Wauben, A. M. Wehman, S. Williams, A. Zendrini, A. J. Zimmerman, C. Théry and K. W. Witwer, *J. Extracell Vesicles*, 2024, **13**, e12404.
8 F. Shekari, F. J. Alibhai, H. Baharvand, V. Börger, S. Bruno, O. Davies, B. Giebel, M. Gimona, G. H. Salekdeh, L. Martin-Jaular, S. Mathivanan, I. Nelissen, E. Nolte-'t Hoen, L. O'Driscoll, F. Perut, S. Pluchino, G. Pocsfalvi, C. Salomon, C. Soekmadji, S. Staubach, A. C. Torrecilhas, G. V. Shelke, T. Tertel, D. Zhu, C. Théry, K. Witwer and R. Nieuwland, *J. Extracell. Biol.*, 2023, **2**, e115.
9 K. Zhang and K. Cheng, *Nat. Rev. Bioeng.*, 2023, **1**, 608–609.
10 J. Zhang, J. Guan, X. Niu, G. Hu, S. Guo, Q. Li, Z. Xie, C. Zhang and Y. Wang, *J. Transl. Med.*, 2015, **13**, 49.
11 Y. Zhang, X. Bai, K. Shen, L. Luo, M. Zhao, C. Xu, Y. Jia, D. Xiao, Y. Li, X. Gao, C. Tian, Y. Wang and D. Hu, *Cells*, 2022, 11.
12 M. Ateeq, M. Broadwin, F. W. Sellke and M. R. Abid, *Med. Sci.*, 2024, 12.
13 M. D. Hade, C. N. Suire, J. Mossell and Z. Suo, *Med. Res. Rev.*, 2022, **42**, 2102–2125.
14 Z. Zakeri, M. Heiderzadeh, A. Kocaarslan, E. Metin, S. N. Hosseini Karimi, S. Saghati, A. Vural, G. Akyoldaş, K. Baysal, Y. Yağcı, Y. Gürsoy-Özdemir, S. Taşoğlu, R. Rahbarghazi and E. Sokullu, *Biomater. Sci.*, 2024, **12**, 2561–2578.
15 Z. Han, L. Dong, A. Li, Z. Li, L. Fu, Z. Zhang, X. Li and X. Li, *Mater. Today Bio*, 2022, **16**, 100427.
16 K. Ulubayram, A. Nur Cakar, P. Korkusuz, C. Ertan and N. Hasirci, *Biomaterials*, 2001, **22**, 1345–1356.
17 Ş. Öztürk, R. Shahbazi, N. D. Zeybek, B. Kurum, M. Gultekinoglu, E. A. Aksoy, M. Demircin and K. Ulubayram, *Biomed. Mater.*, 2021, 16.
18 C. Han, J. Zhou, C. Liang, B. Liu, X. Pan, Y. Zhang, Y. Wang, B. Yan, W. Xie, F. Liu, X. Y. Yu and Y. Li, *Biomater. Sci.*, 2019, **7**, 2920–2933.
19 W. Zhang, L. Jiang, R. J. Diefenbach, D. H. Campbell, B. J. Walsh, N. H. Packer and Y. Wang, *ACS Sens.*, 2020, **5**, 764–771.

20 B. Vestad, A. Llorente, A. Neurauter, S. Phuyal, B. Kierulf, P. Kierulf, T. Skotland, K. Sandvig, K. B. F. Haug and R. Øvstebø, *J. Extracell. Vesicles*, 2017, **6**, 1344087.

21 T. Kahraman, G. Gucluler, I. Simsek, F. C. Yagci, M. Yildirim, C. Ozen, A. Dinc, M. Gursel, L. Ikromzoda, T. Sutlu, S. Gay and I. Gursel, *J. Extracell. Vesicles*, 2017, **6**, 1284449.

22 I. Bártolo, R. L. Reis, A. P. Marques and M. T. Cerqueira, *Tissue Eng Part B Rev*, 2022, **28**, 665–676.

23 C. Dunnill, T. Patton, J. Brennan, J. Barrett, M. Dryden, J. Cooke, D. Leaper and N. T. Georgopoulos, *Int. Wound J.*, 2017, **14**, 89–96.

24 K. Ulubayram, I. Eroglu and N. Hasirci, *J. Biomater. Appl.*, 2002, **16**, 227–241.

25 K. Ulubayram, E. Aksu, S. I. Gurhan, K. Serbetci and N. Hasirci, *J. Biomater. Sci. Polym. Ed.*, 2002, **13**, 1203–1219.

26 C. Bayram, X. Jiang, M. Gultekinoglu, Ş. Öztürk, K. Ulubayram and M. Edirisinghe, *Macromol. Mater. Eng.*, 2019, 304.

27 M. G. Tonnesen, X. Feng and R. A. Clark, *J. Investig. Dermatol. Symp. Proc.*, 2000, **5**, 40–46.

28 K. Bellacen and E. C. Lewis, *J. Vis. Exp.*, 2009, (33), 1564.

29 N. Mangir, S. Dikici, F. Claeyssens and S. MacNeil, *ACS Biomater. Sci. Eng.*, 2019, **5**, 3190–3200.

30 Y. Zhang, Y. Liu, H. Liu and W. H. Tang, *Cell Biosci*, 2019, **9**, 19.

31 S. P. Camões, O. Bulut, V. Yazar, M. M. Gaspar, S. Simões, R. Ferreira, R. Vitorino, J. M. Santos, I. Gursel and J. P. Miranda, *J. Adv. Res.*, 2022, **41**, 113–128.

32 K. Yoo, N. Thapa, J. Lee, Y. Jang, J. O. Lee and J. Kim, *Skin Res. Technol.*, 2023, **29**, e13382.

33 T. Wang, Z. Jian, A. Baskys, J. Yang, J. Li, H. Guo, Y. Hei, P. Xian, Z. He, Z. Li, N. Li and Q. Long, *Biomaterials*, 2020, **257**, 120264.

34 T. Y. Lin, T. M. Chang, W. C. Tsai, Y. J. Hsieh, L. T. Wang and H. C. Huang, *Int. J. Mol. Sci.*, 2023, 24.

35 D. W. Hagey, M. Ojansivu, B. R. Bostancioglu, O. Saher, J. P. Bost, M. O. Gustafsson, R. Gramignoli, M. Svahn, D. Gupta, M. M. Stevens, A. Görgens and S. El Andaloussi, *Sci. Adv.*, 2023, **9**, eadh1168.

36 K. Wu, C. He, Y. Wu, X. Zhou, P. Liu, W. Tang, M. Yu and W. Tian, *Int. J. Nanomed.*, 2021, **16**, 7831–7846.

37 G. Li, Y. Zhang, J. Wu, R. Yang, Q. Sun, Y. Xu, B. Wang, M. Cai, Y. Xu, C. Zhuang and L. Wang, *Front. Bioeng. Biotechnol.*, 2023, **11**, 1096390.

38 X. M. Hu, C. C. Wang, Y. Xiao, P. Jiang, Y. Liu and Z. Q. Qi, *World J. Stem Cells*, 2023, **15**, 947–959.

39 S. Rezaei, M. A. Nilforoushzadeh, M. A. Amirkhani, R. Moghadasali, E. Taghiabadi and D. Nasrabadi, *Mol. Pharm.*, 2024, **21**, 2637–2658.

40 Y. Liu, M. Zhang, C. Wang, H. Chen, D. Su, C. Yang, Y. Tao, X. Lv, Z. Zhou, J. Li, Y. Liao, J. You, Z. Wang, F. Cheng and R. Yang, *ACS Nano*, 2024, **18**, 13696–13713.

41 A. D. F. Ferreira, P. D. S. Cunha, V. M. Carregal, P. C. da Silva, M. C. de Miranda, M. Kunrath-Lima, M. I. A. de Melo, C. C. F. Faraco, J. L. Barbosa, F. Frezard, V. Resende, M. A. Rodrigues, A. M. de Goes and D. A. Gomes, *Stem Cells Int.*, 2017, **2017**, 9841035.

42 M. Wang, C. Wang, M. Chen, Y. Xi, W. Cheng, C. Mao, T. Xu, X. Zhang, C. Lin, W. Gao, Y. Guo and B. Lei, *ACS Nano*, 2019, **13**, 10279–10293.

43 Y. Wang, C. Zhao, R. Guo, T. Xi, J. Xiong and L. Jia, *Skin Res. Technol.*, 2024, **30**, e13694.

44 H. Deng, Y. Jiang, J. Deng, F. Chang, J. Chen, X. Sun, D. Cheng, Z. Wang, R. Li, J. Liu, Y. Li, L. Zhang and P. Yin, *Biomater. Sci.*, 2024, **12**, 1761–1770.

45 D. Hao, H. S. Swindell, L. Ramasubramanian, R. Liu, K. S. Lam, D. L. Farmer and A. Wang, *Front. Bioeng. Biotechnol.*, 2020, **8**, 633.

46 H. González-King, P. G. Rodrigues, T. Albery, B. Tangruksa, R. Gurrapu, A. M. Silva, G. Musa, D. Kardasz, K. Liu, B. Kull, K. Åvall, K. Rydén-Markinhuhta, T. Incitti, N. Sharma, C. Graneli, H. Valadi, K. Petkevicius, M. Carracedo, S. Tejedor, A. Ivanova, S. Heydarkhan-Hagvall, P. Menasché, J. Synnergren, N. Dekker, Q. D. Wang and K. Jennbacken, *J. Extracell. Vesicles*, 2024, **13**, e12445.

47 D. Ribatti, A. Gualandris, M. Bastaki, A. Vacca, M. Iurlaro, L. Roncali and M. Presta, *J. Vasc. Res.*, 1997, **34**, 455–463.

48 J. Ma, Y. Zhao, L. Sun, X. Sun, X. Zhao, X. Sun, H. Qian, W. Xu and W. Zhu, *Stem Cells Transl. Med.*, 2017, **6**, 51–59.

49 G. Merckx, B. Hosseinkhani, S. Kuypers, S. Deville, J. Irobi, I. Nelissen, L. Michiels, I. Lambrichts and A. Bronckaers, *Cells*, 2020, **9**(2), 312.